



# Vibro-acoustic and buckling analysis of a thermal plate-cavity coupled system

Qing Luo<sup>a</sup>, Yanfeng Wang<sup>b</sup>, Yukang Yang<sup>a</sup>, Qi Xu<sup>a,\*</sup>, Yinghui Li<sup>a</sup>, Li Cheng<sup>c</sup>

<sup>a</sup> School of Mechanics and Aerospace Engineering, Southwest Jiaotong University 610031, Chengdu, China

<sup>b</sup> Sichuan Gas Turbine Establishment, Aero Engine Corporation of China, Chengdu 610500, China

<sup>c</sup> Department of Mechanical Engineering, the Hong Kong Polytechnic University, Hong Kong, China

## ARTICLE INFO

### Keywords:

Plate-acoustic system  
Thermal effect  
Rayleigh–Ritz method  
Vibro-acoustic characteristics  
Buckling behavior

## ABSTRACT

In this paper, the vibro-acoustic and buckling characteristics of a rectangular plate-acoustic cavity system under thermal loads are studied. Both the structure material and the internal acoustic field are assumed to be temperature-dependent, with the acoustic cavity consisting of impedance walls. Considering the interaction between the structure and the acoustic cavity, the governing equations of the coupled system are derived and solved via the improved Fourier series and the Rayleigh–Ritz method. Vibro-acoustic modes in such a coupled system are strongly affected by the coupling among subsystems. With thermal loads being considered, we observe that this strong coupling effect can be triggered more easily, even for thick plates or relatively large cavities. To address this, a simplified formulation for the coupled fundamental mode is also given following the fully coupled modeling procedures. Also, it is found that coupling the plate with a cavity can delay the onset of structural buckling. Therefore, for strongly coupled systems, the buckling temperature of the substructure may be much higher than for uncoupled or only weakly coupled substructures, which may enhance the safety of the system in a thermal environment.

## 1. Introduction

Systems consisting of elastic sub-structures and internal cavities are commonly seen in engineering. The vibro-acoustic interactions between the structural vibration and sound field inside the cavity may cause noise problems or even damage the system structure, especially for systems working in extreme thermal or magnetic environments [1–3]. Also, as the environment changes, sub-structures comprising elastic structures like plates or shells may become unstable and buckled [4–6]. Though buckling is usually considered as a static problem, it actually involves the instability of related vibration modes of the system. In this paper, we study the vibro-acoustics of a typical structural-acoustic system in a thermal environment, with buckling also being considered.

In the theoretical, to model and study the vibro-acoustic characteristics, a structural-acoustic system is generally divided into two coupled subsystems: the structure part and the cavity part [7]. The two subsystems are dynamically coupled with each other through interactions at the mutual interface. In this regard, the modal coupling method first studies the subsystem modes and then assembles these sub-modes by means of calculating the acoustic-vibration modal coupling coefficient

[8,9]. Also, improved modal coupling methods, like the dual-modal coupling method [10,11] and the modal reduction method [12,13] have been proposed and widely used. Similarly, the energy-based methods calculate the energies of the subsystems, and derive the governing equations via applying the variational principle to the assembled total energy. Typical energy-based methods include but are not limited to the variational-based method (VBM) [14,15], the static energy analysis (SEA) [16–20], the improved Fourier series method (IFSM) [21–25], the Chebyshev polynomial method (CPM) [26–28] and so on. Compared with the modal coupling methods, the energy-based methods are often more accurate, especially for cases involving strong structural-cavity interactions. Numerical methods like the finite element method (FEM) [29,30], boundary element method (BEM) [31–33], spectral element method (SEM) [34,35], wave finite element method (WEM) [36,37], and so on, are also popular to tackle the structural-cavity systems, where the structural-cavity interactions can be directly considered in the finite element formulation. With good suitability for systems of geometry irregularity, numerical methods may have low computational efficiency or convergence difficulty in certain frequency ranges. For example, an enormous element meshing is needed for FEM and BEM for

\* Corresponding author.

E-mail address: [xuqi@swjtu.edu.cn](mailto:xuqi@swjtu.edu.cn) (Q. Xu).

<https://doi.org/10.1016/j.ijmecsci.2023.108789>

Received 4 June 2023; Received in revised form 27 September 2023; Accepted 30 September 2023

Available online 1 October 2023

0020-7403/© 2023 Elsevier Ltd. All rights reserved.

high-frequency simulations, resulting in a high computational cost and memory resources [38,39].

Structural-cavity systems may exhibit weak or strong coupling effects, depending on how much the interactions between subsystems affect the system modes. For a weakly coupled system, the interactions between subsystems have little influence on the system modes, and can even be ignored for simplicity. In such a case, the system modes are generally close to the modes of the subsystems [40,41]. However, for a strongly coupled system, like a thin and flexible structure coupled with a shallow cavity or a cavity filled with a high-density medium, the modal behaviors of the coupled system are quite different from those of the subsystems, and cannot be directly predicted by the subsystem. Based on the structural modes and the rigid acoustic cavity modes, the coupling coefficient between different structure modes and the acoustic cavity modes can be approximately obtained to evaluate the degree of spatial coupling [42–45]. To solve strongly coupled systems, the classical modal coupling method may not converge well, especially for coupled subsystems involving both high- and low-frequency modes [46]. In this regard, the pseudo-static correction method [47] is proposed for modal coupling analysis of strongly coupled systems. Also, other analytical and semi-analytical methods like the patch transfer functions method [48], decoupled modal projection method [49], coupled reduced-order modeling technique [50], and so on, have been adopted.

On the other hand, with a demanding requirement for structural vibro-acoustic performance, many advanced structural-cavity systems work in tough thermal environments. For example, the surface of high-speed aircraft endures a temperature of 350 °C caused by friction at a 3 Mach speed [51], and underwater vehicles are exposed to great temperature drops when diving [52]. The heat transfer processes, either in transient or steady state, can be categorized as thermal radiation, convective heat transfer, and heat conduction. These processes involve key principles and properties that are important for understanding the heat transfer dynamics, for example, the heat transfer rate like heat flux and heat flux density [53,54], the blackbody radiation principles [55], Newton's cooling law [56,57] and Prandtl number [58] in convection, Fourier thermal conductive law [59], and so on. Heat transfer processes also induce various structural and acoustic vibrations. For instance, the spacecraft's solar panel endures cyclic solar thermal radiation due to the day-night transitions, leading to periodic thermal excitations that cause structural vibrations [60,61]. The convective heat transfer and thermal radiation in combustion chambers may couple with the acoustic modes of the system, and hence generates thermoacoustic oscillations that can affect the combustion efficiency or even cause structural damage [62, 63]. The heat transfer processes also affect the properties of both the structural material and cavity medium, and consequently the mechanical properties of the system. For example, the temperature rise/drop of the structural-cavity systems can greatly affect the vibro-acoustic modes and responses of structural-cavity systems. As the temperature goes up, the sound is easier to spread in the low-frequency region, as the peaks of the sound transmission loss will drop and float to lower frequencies [64–66]. The mode shift phenomenon may also occur under thermal loads. With continued heating, the inherent vibro-acoustic modes of a system may shift between each other, and may lead to unwanted vibration mode shapes in the system [67,68]. System instability may also be triggered due to the thermal load, leading to the so-called thermal buckling [5,69] or thermal flutter [70], depending on whether the frequency of the unstable modes is zero or not [71].

In this paper, the vibro-acoustic and buckling characteristics of a rectangular plate-cavity system under steady-state thermal loads are studied, focusing on the elucidation of weak/strong coupling effects and how they affect vibro-acoustics and thermal buckling. The thermal effect is encompassed in the description of the acoustic medium properties, and the plate displacement field by using the classical plate theory (CPT) [72–74]. The improved Fourier series method (IFSM) and the Rayleigh–Ritz method are then adopted to model and solve the coupled thermal system, considering a class of general boundary conditions and

impedance walls. Owing to its energy-based feature, this combination of methods shows good convergence and accuracy, and enables detailed parametric study of thermal weak/strong coupling. We show that the weak/strong coupling effect affects the dynamical and buckling behavior of the system quite differently. Through case studies and the derivation of a simplified formula for the coupled fundamental mode, we explain how the strong coupling effect, via changing the structural geometry or the cavity-medium property, delays the onset of the structural buckling.

The rest of the paper is arranged as follows. In Section 2, the governing equation of the coupled system is developed and solved. Section 3 validates the proposed method via solutions existing in the literature, and carries out a parametric study of the buckling and vibro-acoustic modes, in terms of weak/strong coupling characteristics and thermal effect. Finally, in Section 4, conclusions are drawn.

## 2. Theoretical modeling

In this work, an isotropic and rectangular plate coupled with a regular cavity is investigated, as shown in Fig. 1. The length and width of the plate and the cavity are the same, and denoted by  $a$ ,  $b$ . The thickness of the plate is  $h_p$ , and the depth of the cavity is  $h_c$ . The boundary condition of the plate is simply supported, while those of the acoustic cavity is of arbitrary impedance. An orthogonal coordinate system  $Oxyz$  is used, with the middle plane of the plate being the  $Oxy$  plane, and  $z$ -direction alongside the cavity depth  $h_c$ . As the plate is thin, it is assumed to be of uniform temperature, which takes the form of  $T = T_0 + \Delta T_p$ , where  $T_0$  denotes the initial (free stress) temperature of the plate and  $\Delta T_p$  is the temperature rise. The temperature of the acoustic cavity is represented by  $T_c = T_0 + \Delta T_c$ , which may be the same as the plate temperature or not.

The displacement components of the plate at an arbitrary point in the  $x$ ,  $y$ , and  $z$  directions are denoted  $U(x,y,z,t)$ ,  $V(x,y,z,t)$ , and  $W(x,y,z,t)$ , respectively. The sound pressure inside the coupled system is denoted as  $p(x,y,z,t)$ . In the following discussions,  $U(x,y,z,t)$ ,  $V(x,y,z,t)$ ,  $W(x,y,z,t)$ , and  $p(x,y,t)$  are abbreviated as  $U$ ,  $V$ ,  $W$ , and  $p$  for simplification. The vibration characteristics of the plate-cavity system are then studied, by considering the mutual interactions between the vibrating plate and the acoustic waves inside the cavity.

### 2.1. Basic equations

According to the classical thin plate theory (without considering shear deformation along the  $z$ -direction), the displacement field of an arbitrary point of the plate and the strain components can be expressed as [75]

$$\begin{cases} U = u_0 - z \frac{\partial w_0}{\partial x}, \varepsilon_{xx} = \frac{\partial u_0}{\partial x} - z \frac{\partial^2 w_0}{\partial x^2}, \\ V = v_0 - z \frac{\partial w_0}{\partial y}, \varepsilon_{yy} = \frac{\partial v_0}{\partial y} - z \frac{\partial^2 w_0}{\partial y^2}, \\ W = w_0, \gamma_{xy} = \frac{\partial u_0}{\partial y} + \frac{\partial v_0}{\partial x} - 2z \frac{\partial^2 w_0}{\partial x \partial y}, \end{cases} \quad (1)$$

in which  $u_0$ ,  $v_0$ , and  $w_0$  are the middle surface displacements of the rectangular plate.

Considering the thermal effect of the plate, the stress of an arbitrary point of the plate is given by [76]

$$\begin{Bmatrix} \sigma_{xx} \\ \sigma_{yy} \\ \sigma_{xy} \end{Bmatrix} = \begin{Bmatrix} \sigma_{xx}^0 \\ \sigma_{yy}^0 \\ \sigma_{xy}^0 \end{Bmatrix} - \begin{Bmatrix} \sigma_{xx}^T \\ \sigma_{yy}^T \\ \sigma_{xy}^T \end{Bmatrix} = \begin{bmatrix} Q_{11} & Q_{12} & 0 \\ Q_{21} & Q_{22} & 0 \\ 0 & 0 & Q_{66} \end{bmatrix} \begin{Bmatrix} \varepsilon_{xx} - \alpha(T - T_0) \\ \varepsilon_{yy} - \alpha(T - T_0) \\ \varepsilon_{xy} \end{Bmatrix}, \quad (2)$$

in which  $Q_{ij}$  ( $i, j = 1, 2, 6$ ) is the material stiffness coefficients relating

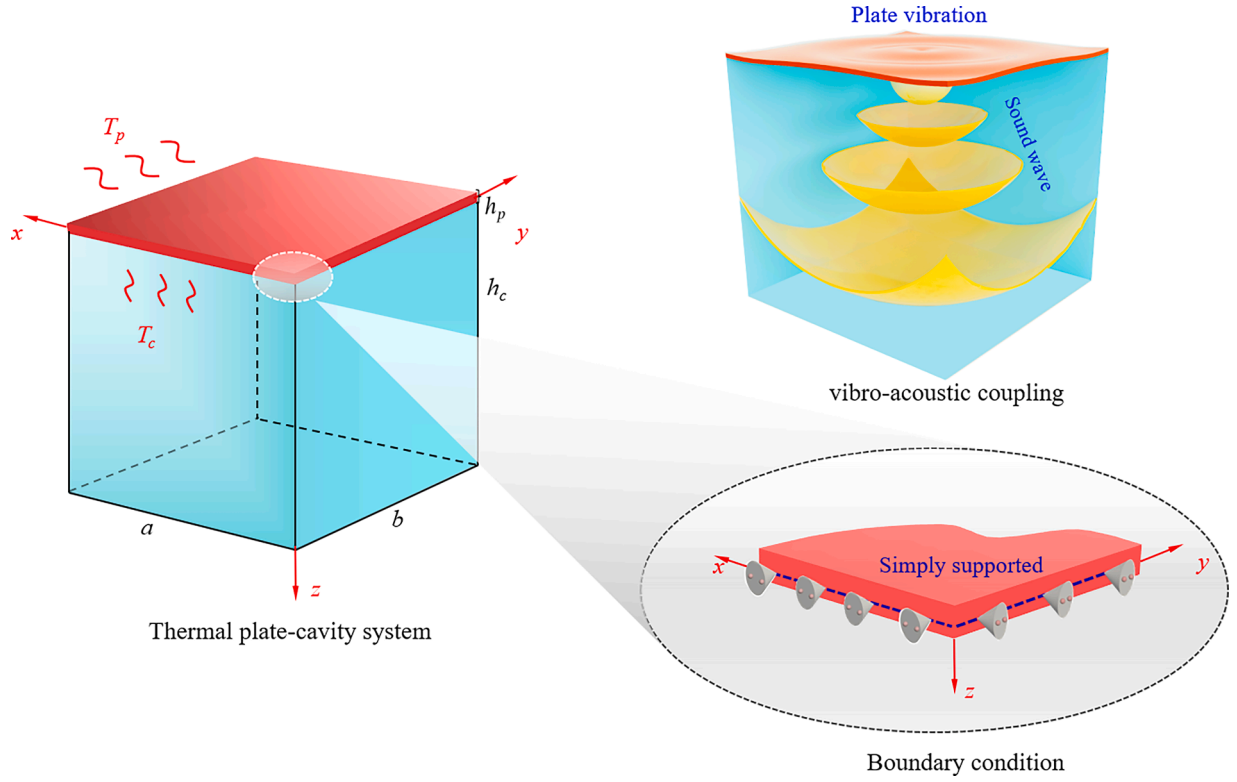


**Fig. 1.** A rectangular plate-cavity system in a thermal environment. The length, width, and thickness of the plate are  $a$ ,  $b$ ,  $h_p$ , and the depth of the cavity is  $h_c$ . The plate and the cavity are subjected to thermal loads, denoted as  $T_p$  and  $T_c$ , respectively. The vibro-acoustic coupling between the plate vibrations and sound waves, as well as the simply supported plate boundary condition, are also shown in this figure.

to Young's modulus ( $E$ ) and Poisson's ratio ( $\nu$ ) of the plate, the specific expression of  $Q_{ij}$  is given in [Appendix B](#). It should be noticed that  $E$ ,  $\nu$ , and other parameters including the thermal expansion coefficient  $\alpha$  and the mass density  $\rho_p$  used in the following sections are all functions of temperature  $T$ , which can be approximated as a series of  $T$  as [\[77\]](#)

$$\Gamma(T) = \Gamma_0(\Gamma_{-1}T^{-1} + 1 + \Gamma_1T + \Gamma_2T^2 + \Gamma_3T^3), \quad (3)$$

where  $\Gamma$  denotes the temperature-dependent parameter, and constants  $\Gamma_{-1}$ ,  $\Gamma_0$ ,  $\Gamma_1$ ,  $\Gamma_2$ ,  $\Gamma_3$  are the coefficients relating to each specific parameter as  $\Gamma_0$  denotes the free stress state coefficient of the plate.

## 2.2. Energy functional of the coupled system

Considering the coupling effect of the acoustic cavity, the Lagrange equation of the rectangular plate and the acoustic cavity can be written as [\[78\]](#)

$$\begin{aligned} L_P &= U_P - T_P + W_{C-P} - U_T, \\ L_C &= U_C - T_C - W_{P-C} - W_{wall}, \end{aligned} \quad (4)$$

where  $U_P$ ,  $T_P$ ,  $U_C$ , and  $T_C$  are the potential and kinetic energies of the plate and the acoustic cavity, respectively;  $U_T$  is the strain energy due to temperature rise;  $W_{C-P}$  is the work done by the sound pressure of the acoustic cavity, and  $W_{wall}$  is the energy dissipated at the impedance walls except the plate surface. The basic energy expressions of the coupled system are given in [Appendix A](#).

Specifically, the potential energy  $U_T$  due to temperature rise can be expressed as [\[79\]](#)

$$U_T = \frac{1}{2} \int_0^a \int_0^b \int_{-h_p/2}^{h_p/2} (\sigma_{xx}^T d_{xx} + 2\sigma_{xy}^T d_{xy} + \sigma_{yy}^T d_{yy}) dx dy dz, \quad (5)$$

where  $d_{ij}$  is the strain component due to temperature rise, and can be

seen in literature [\[80\]](#)

The work  $W_{C-P}$  is the surface integral of the displacement of an area element of the plate surface times its acoustic pressure, which takes the form of

$$W_{C-P} = \int_s p \left[ u_0 + v_0 + w_0 - z_e \left( \frac{\partial w_0}{\partial x} + \frac{\partial w_0}{\partial y} \right) \right] ds, \quad (6)$$

where  $z_e$  denotes the coordinate of the coupling surface in the  $z$ -direction.

Due to the thermal loads on the acoustic cavity, the medium properties, i.e., the mass density  $\rho_c$ , and the sound speed  $c_0$ , are temperature dependent, which take the form of

$$\rho_c = \frac{P_0}{0.2869(T_c + T_c^0)} \text{ (kg/m}^3\text{)}, \quad (7)$$

$$c_0(T_c) = 331.4 + 0.607T_c \text{ (m/s)}, \quad (8)$$

where  $P_0$  is the atmospheric pressure,  $T_c^0 = 273.15$  °C is the absolute temperature zero. In the context of a coupled system within a non-enclosed cavity, material exchange occurs between the cavity's internal medium and the external environment, resulting in temperature-dependent in density and sound velocity.

## 2.3. Admissible displacement field and sound pressure by Fourier series

Consider simply supported boundary conditions for the plate. The displacement field of the plate should satisfy the boundary condition and can be simulated by using the Fourier series, which writes

$$\begin{cases} u_0 = \left[ \sum_{m=0}^{\infty} \sum_{n=0}^{\infty} A_{mn} \sin(\lambda_{am}x) \cos(\lambda_{bn}y) \right] e^{-j\omega t}, \\ v_0 = \left[ \sum_{m=0}^{\infty} \sum_{n=0}^{\infty} B_{mn} \cos(\lambda_{am}x) \sin(\lambda_{bn}y) \right] e^{-j\omega t}, \\ w = \left[ \sum_{m=0}^{\infty} \sum_{n=0}^{\infty} C_{mn} \sin(\lambda_{am}x) \sin(\lambda_{bn}y) \right] e^{-j\omega t}, \end{cases} \quad (9)$$

in which  $\lambda_{am} = \frac{m\pi}{a}$ ,  $\lambda_{bn} = \frac{n\pi}{b}$ ,  $j$  is the imaginary unit, and  $\omega$  is the natural frequency of the coupled system, and  $A_{mn}$ ,  $B_{mn}$ , and  $C_{mn}$  are the Fourier coefficients of modal shapes to be solved.

Similarly, to satisfy the arbitrary impedance walls [81,82], the sound pressure  $p$  is assumed as a superposition of a 3D Fourier series and six polynomial functions, and  $p$  can be expressed as [83]

$$p = \left\{ \begin{aligned} & \sum_{m_1=0}^{\infty} \sum_{n_1=0}^{\infty} \sum_{l_1=0}^{\infty} D_{m_1 n_1 l_1} \cos(\lambda_{am_1}x) \cos(\lambda_{bn_1}y) \cos(\lambda_{h_c l_1}z) \\ & + \sum_{m_1=0}^{\infty} \sum_{n_1=0}^{\infty} [\xi_1(z) D_{m_1 n_1}^1 + \xi_2(z) D_{m_1 n_1}^2] \cos(\lambda_{am_1}x) \cos(\lambda_{bn_1}y) \\ & + \sum_{m_1=0}^{\infty} \sum_{l_1=0}^{\infty} [\xi_1(y) D_{m_1 l_1}^3 + \xi_2(y) D_{m_1 l_1}^4] \cos(\lambda_{am_1}x) \cos(\lambda_{h_c l_1}z) \\ & + \sum_{n_1=0}^{\infty} \sum_{l_1=0}^{\infty} [\xi_1(x) D_{n_1 l_1}^5 + \xi_2(x) D_{n_1 l_1}^6] \cos(\lambda_{bn_1}y) \cos(\lambda_{h_c l_1}z) \end{aligned} \right\} e^{-j\omega t}, \quad (10)$$

where  $\lambda_{am_1} = \frac{m_1\pi}{a}$ ,  $\lambda_{bn_1} = \frac{n_1\pi}{b}$ , and  $\lambda_{h_c l_1} = \frac{l_1\pi}{h_c}$ . The auxiliary functions  $\xi_1(s)$  and  $\xi_2(s)$  ( $s = x, y, z$ ) introduced there is a supplement to sound pressure  $p$ , to eliminate the discontinuities in acoustic walls and can be seen in literature [83].

#### 2.4. Solution procedure

The governing equations of the coupled system can be derived by the Rayleigh–Ritz method. More specifically, taking partial derivatives of both  $L_P$  and  $L_C$  against corresponding Fourier coefficients, and equating the results to zero, it derives that

$$\frac{\partial L_P}{\partial \Theta_{mn}} = \frac{\partial U_P}{\partial \Theta_{mn}} - \frac{\partial T_P}{\partial \Theta_{mn}} + \frac{\partial W_{C-P}}{\partial \Theta_{mn}} - \frac{\partial U_T}{\partial \Theta_{mn}} = 0, \quad (11)$$

$$\frac{\partial L_C}{\partial \Phi_{m_1 n_1 l_1}} = \frac{\partial U_C}{\partial \Phi_{m_1 n_1 l_1}} - \frac{\partial T_C}{\partial \Phi_{m_1 n_1 l_1}} - \frac{\partial W_{P-C}}{\partial \Phi_{m_1 n_1 l_1}} - \frac{\partial W_{wall}}{\partial \Phi_{m_1 n_1 l_1}} = 0. \quad (12)$$

Substituting energy expression of the coupled system into Eqs. (11) and (12), the governing equation of the system can then be written in matrix form as

$$\begin{bmatrix} K_P - \omega^2 M_P & C_{C-P} \\ \omega^2 C_{P-C} & K_C - \omega Z_C - \omega^2 M_C \end{bmatrix} \begin{bmatrix} \Theta \\ \Phi \end{bmatrix} = \begin{bmatrix} 0 \\ 0 \end{bmatrix}, \quad (13)$$

where  $K_P$ ,  $M_P$ ,  $K_C$ , and  $M_C$  are the stiffness or mass matrix of the plate and the acoustic cavity;  $Z_C$  is the impedance matrix derived from  $W_{wall}$  (due to the dissipative effect of the walls);  $C_{C-P}$  and  $C_{P-C}$  are the coupling matrices satisfying  $C_{C-P} = C_{P-C}^T$  due to  $W_{C-P} = W_{P-C}$ ;  $\Theta$  and  $\Phi$  are vectors of undetermined coefficients of the displacement field and the sound pressure field. Detailed expressions for these matrices are given in Appendix B, where the Fourier series are truncated to  $m = M_p$ ,  $n = N_p$ , and  $m_l = M_c$ ,  $n_l = N_c$ ,  $l_l = L_c$  for the convenience of numerical calculation.

Obviously, the natural frequencies and eigenvectors of the coupled system can be solved by letting

$$\det \begin{bmatrix} K_P - \omega^2 M_P & C_{C-P} \\ \omega^2 C_{P-C} & K_C - \omega Z_C - \omega^2 M_C \end{bmatrix} = 0. \quad (14)$$

### 3. Numerical results and discussion

This section carries out several numerical examples, including verification examples of buckling and vibration of individual subsystems in the first subsection, and fully coupled thermal plate-cavity system in the following subsections. The temperatures of the plate and acoustic medium are the same, i.e.,  $\Delta T_c = \Delta T_p$ . The plate is assumed to be isotropic and is set as SUS304, whose temperature-dependent material properties are referred to in reference [84]. Unless otherwise stated, the cavity is non-enclosed with air medium, and the default values of the plate length and width are fixed as  $a \times b = 0.4 \text{ m} \times 0.4 \text{ m}$ .

#### 3.1. Buckling and vibration modes of subsystems

First, the thermal effect on the buckling of the plate is studied. As the temperature rises, the equivalent stiffness of the plate drops, and the buckling would be triggered. Fig. 2(a) gives the critical buckling temperature rise (CTR) of plates of different geometry, by setting the equivalent stiffness  $K_p$  as zero. Altogether, the CTR of the plate decreases as the plate becomes thinner or slimmer, in line with common understandings. Secondly, the vibro-acoustic modal frequency  $\omega$  of a pure acoustic cavity is studied for verification. The acoustic cavity is set to be at room temperature. Fig. 2(b) displays the calculated first-order  $\omega$  versus the cavity depth  $h_c$ , with different cavity lengths  $a$ . It is seen that  $\omega$  can be divided into two stages. The first stage is for  $h_c < a$ , where  $\omega$  is flat. The second stage is  $h_c > a$ , where  $\omega$  decreases exponentially as  $h_c$  grows. To explain this, Fig. 2(c) gives the first six orders  $\omega$  for fixed  $a = 0.4 \text{ m}$ , where the logarithmic coordinate system is adopted to better display  $\omega$  when the cavity depth is shallow. From this figure, the first six orders of  $\omega$  actually are composed of different frequency branches of the acoustic cavity through the mode shift phenomenon [85,86]. For example, the first order  $\omega$  begins with the constant  $S(1,0,0)/S(0,1,0)$  (the first-order mode dominated by cavity length or width, which is constant as  $a/b$  is fixed), then intersects with the  $S(0,0,1)$  (the first-order mode dominated by  $h_c$ , which exponentially decreases with  $h_c$ ), and finally follows  $S(0,0,1)$  for  $h_c > 0.4 \text{ m}$  since  $S(0,0,1)$  is smaller. The other orders  $\omega$  are also plotted in Fig. 2(c). Similar to the first order  $\omega$ , these orders  $\omega$  are firstly flat, and then decrease exponentially as  $h_c$  grows, due to the mode shift phenomenon. Other convergence analyses of the proposed method are also carried out and presented in Tables 1–3, as referred to in Appendix C.

#### 3.2. Thermal effect on the coupled modes of the system

This subsection investigates the modes characteristics of a fully coupled thermal plate-cavity system. First, in Fig. 3(a), the first four orders of the coupled  $\omega$  versus  $h_c$  at room temperature are plotted. The plate is simply supported, and the cavity walls except the coupling interface are acoustically rigid, and  $a = b = 0.4 \text{ m}$ . As  $h_c$  grows, these orders  $\omega$  may increase, remain flattened, or decrease exponentially. And they also intersect with each other, as a so-called mode shift phenomenon. Take the first-order  $\omega$  for example, when  $h_c$  is very small,  $\omega$  resembles neither that of the plate nor the pure acoustic cavity, indicating the coupling effect is strong. At  $h_c = 0.0012 \text{ m}$ ,  $\omega$  intersects with  $S(0,1,0)/S(1,0,0)$  and follows it. At  $h_c = 0.4 \text{ m}$ ,  $\omega$  intersects with  $S(0,0,1)$  and follows it at an exponentially decreasing rate. Thus for  $h_c > 0.0012 \text{ m}$ , the coupling effect can be regarded as very weak, and can be respectively considered as cavity-controlled.

For plate-cavity coupled systems of thinner plate thickness, as shown in Fig. 3(b)–(d), the strong coupling effect is more obvious for a relatively large range of  $h_c$ . For instance, there is a strong coupled frequency

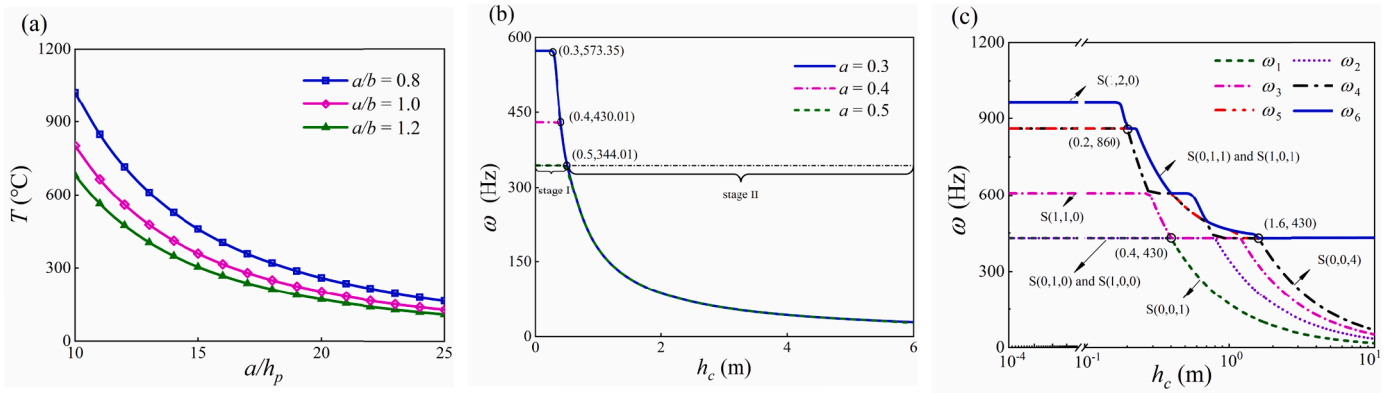


Fig. 2. Buckling and vibro-acoustic modes of the subsystem: (a) Critical buckling temperature rise of a plate; (b) First order modal frequency of a pure cavity, with respect to the cavity depth  $h_c$ ; (c) First six orders of mode frequencies of a pure cavity with respect to  $h_c$ .  $S(n_x, n_y, n_z)$  represents the acoustic modes with  $n_x, n_y, n_z$  being the modal orders along spatial directions.

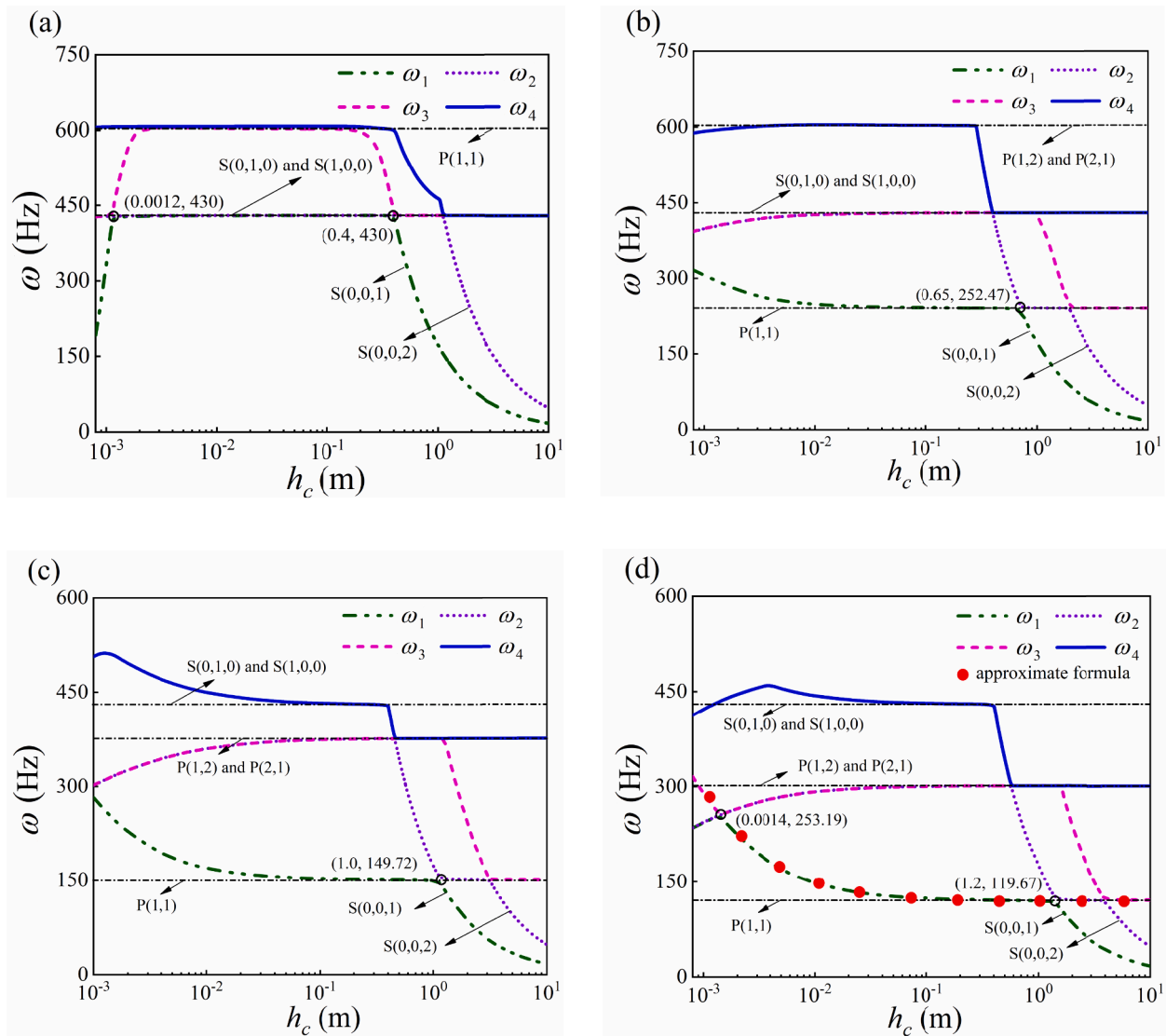


Fig. 3. Effect of the cavity depth  $h_c$  on  $\omega$  of the coupled system at room temperature, with different plate thickness: (a)  $a/h_p = 20$ ; (b)  $a/h_p = 50$ ; (c)  $a/h_p = 80$ ; (d)  $a/h_p = 100$ . The red dots are the results calculated by approximate theoretical formula, and the black dash lines represent the plate frequencies  $\omega$  in-vacuo  $P(i, j)$  or pure acoustic modes  $S(n_x, n_y, n_z)$ .

branch (green dashed line in Fig. 3(b) and (c), or first pink and green dashed line in Fig. 3(d)) that decreases gradually to  $P(1,1)$ . Hence due to the mode shift phenomenon, the first-order coupled  $\omega$  goes through a decreasing pattern (Fig. 3(b) and Fig. 3(c)), or a first-increase-then-decrease pattern (Fig. 3(d)) at the strong coupling stage, and becomes a weakly coupled frequency that is plate-controlled, and eventually becomes cavity controlled. Comparing Fig. 3(a) with Fig. 3(c), (d), for systems of the thicker plate, the weak coupling stage may not have the plate-controlled stage, indicating that a thick-plate coupled system resembles more like a pure acoustic cavity. In addition, it is seen in Fig. 3 (c) and (d) that  $\omega_4$  varies non-monotonically with cavity depth. This is because  $\omega_4$  intersects with higher orders of  $\omega$  at a certain cavity depth, and only  $\omega_4$  is kept in these subfigures.

Similarly to Fig. 3, the first four orders coupled  $\omega$  are plotted in Fig. 4, considering different temperature rise  $\Delta T$ . The dimension of the plate is fixed as  $a = b = 0.4$  m,  $a/h_p = 50$ . Compared with Fig. 3, a similar trend of the strong and weak coupling stages is observed in Fig. 4, but different orders of the system are affected quite differently by  $\Delta T$ . Specifically, increasing  $\Delta T$  leads to the reduction of the values of the first and fourth orders  $\omega$  that are plate-controlled (they respectively stabilize to  $P(1,1)$  and  $P(1,2)$ ), while the values of the second and third cavity-

controlled basically do not change. This indicates that, such a magnitude of temperature rise affects the plate much more greatly than the acoustic cavity. As a result, when  $h_c$  is in the middle range, the difference between the values of the first- and second-order frequencies is greatly amplified by the temperature rise. For a large enough  $h_c$ , whose threshold is the intersection value of  $P(1,1)$  and  $S(0,0,1)$ , the lower modes are all cavity-controlled and are not affected much by the temperature rise.

An effort is made to develop simple tools to understand and even predict some of the salient modal frequency changes observed from the fully coupled analysis. To this end, by assuming that only the rigid cavity mode affects the system, the first-order coupled frequency of the system can be approximated by [87]

$$\omega_c^2(T) = \omega_v^2(T) + \frac{\rho_c(T)c_0^2(T)SL_{p0}^2}{M_p h_c}, \quad (15)$$

where  $\omega_v = \omega_{p(1,1)}$  is the fundamental plate mode in vacuum,  $M_p$  is the generalized modal mass of the plate, and  $L_{p0}$  is the coupling coefficient defined as

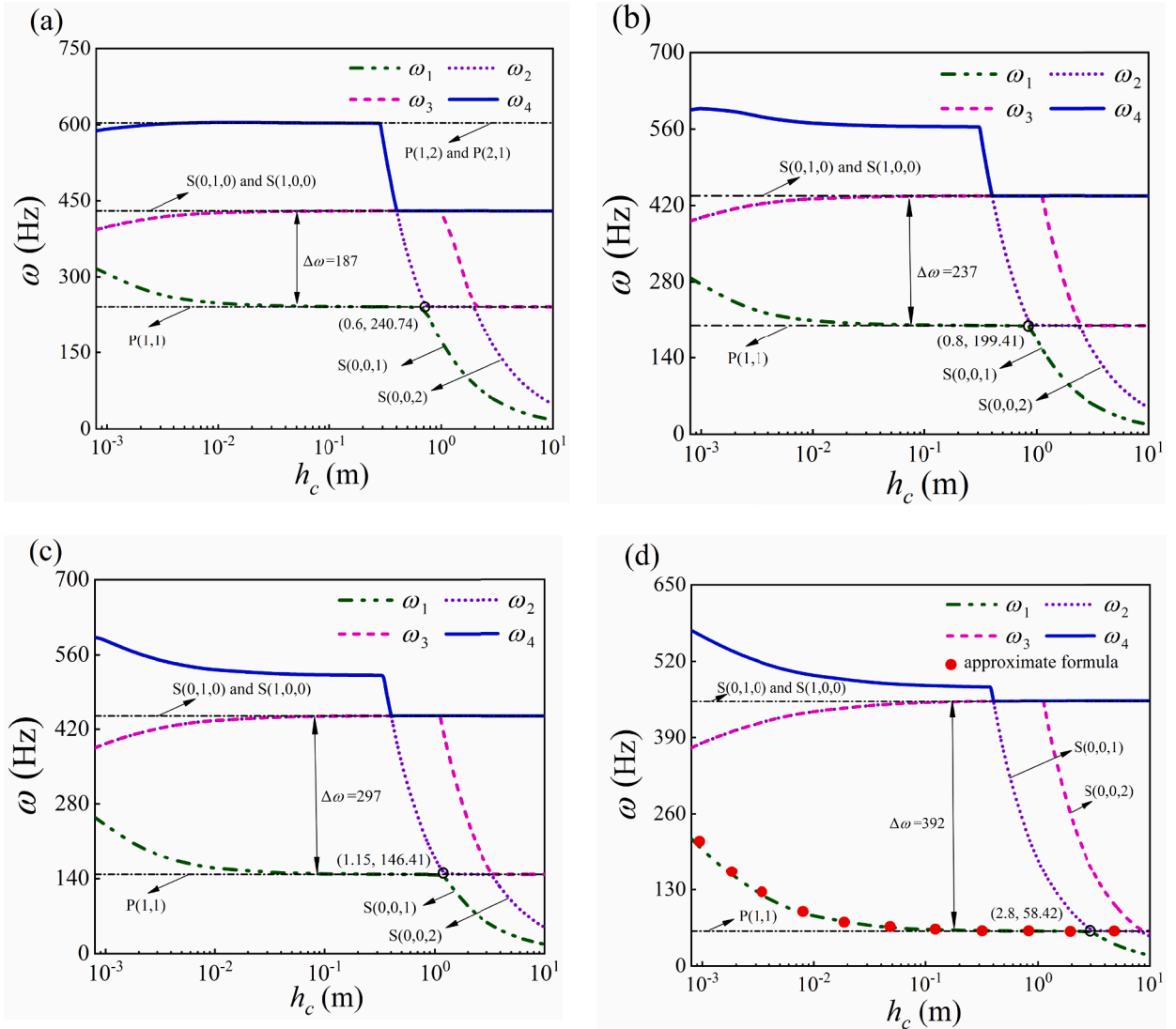


Fig. 4. Effect of the cavity depth  $h_c$  on  $\omega$  of the coupled system for  $a/h_p = 50$ , with different temperature rise: (a)  $\Delta T = 0^\circ\text{C}$ ; (b)  $\Delta T = 10^\circ\text{C}$ ; (c)  $\Delta T = 20^\circ\text{C}$ ; (d)  $\Delta T = 30^\circ\text{C}$ . The red dots are the result calculated by the approximate formula, and the black dash lines represent the plate frequencies in-vacuo  $P(i, j)$  or pure acoustic modes  $S(i, j, k)$ .

$$L_{p0} = \frac{1}{S} \int_S \prod_p \Psi_c ds,$$

with  $\Pi_p$  and  $\psi_c$  being the rigid cavity mode shape and the fundamental plate mode shape in vacuum.  $S$  is the area of the coupling interface. From the approximate formula (15), for plate-cavity systems with only  $h_c$  growing, the aerostatic part of  $\omega_c$  decreases inverse proportionally, thus  $\omega_c$  decreases gradually and eventually approaches  $\omega_v$ . Figs. 3(d) and 4(d) respectively plot the results of Eq. (15) in red solid circles, showing that the approximate formula agrees very well with the plate-controlled mode for the given systems. Eq. (15) not only enables effective prediction of the changes in the fundamental plate-controlled frequency under thermal loads, but also provides an intuitive understanding on how this mode changes with system parameters. For instance, the righthand-side term of Formula (15) gives a rough estimation of the weak/strong coupling effect for a given cavity depth or structural thickness. However, the mode calculated by Eq. (15) is not necessarily the first-order one of the system. To obtain the exact orders of the modes, other modes need to be calculated and the mode shift phenomenon ought to be considered too.

### 3.3. Thermal buckling of the plate in the coupled system

To further reveal the thermal effect of the coupled system, this subsection discusses the buckling behaviors. First in Fig. 5, the effect of  $\Delta T$  on the first four orders  $\omega$  is shown for a coupled system of  $a/h_p = 20$ , wherein each sub-figure,  $h_c$  is chosen differently so that the system is strongly Fig. 5(a)–(c) or weakly (Fig. 5(d)–(f)) coupled. When  $\Delta T$  grows, the plate/cavity-controlled  $\omega$  decreases/increases monotonously. Compared to Fig. 4 where the temperature does not affect the cavity-controlled  $\omega$ , here the cavity-controlled  $\omega$  increases with  $\Delta T$  since the temperature rise is much larger. For strong coupling cases, the value of plate/cavity-controlled  $\omega$  varies quite much, in accordance with Fig. 4. For all sub-figures, the plate-controlled  $\omega$  becomes the first-order mode

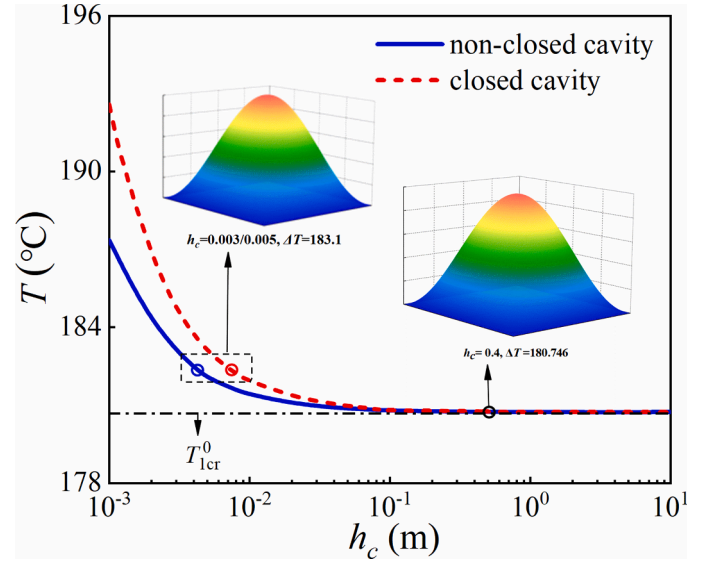


Fig. 6. Effect of the cavity depth  $h_c$  on the critical buckling temperature rise of the coupled system with  $a/h_p = 20$ , for both the enclosed and non-enclosed cases. The black dash line indicates the critical buckling temperature rise of the subsystem plate.

of the coupled system, and finally decreases to zero. Fig. 6 plots the CTR when the plate-controlled  $\omega$  becomes zero for systems with non-enclosed or enclosed cavity (in both cases the medium is considered as an ideal gas), where the CTR slowly decreases with  $h_c$ , and eventually stabilizes to a constant value. Actually, this constant value is very close to the first-order CTR of the corresponding sub-plate ( $P(1,1)$ ), and is denoted as  $T_{cr}^1$  here. Fig. 6 also shows that in the case of an enclosed cavity, the CTR significantly increases when  $h_c$  is not large. According to the simplified

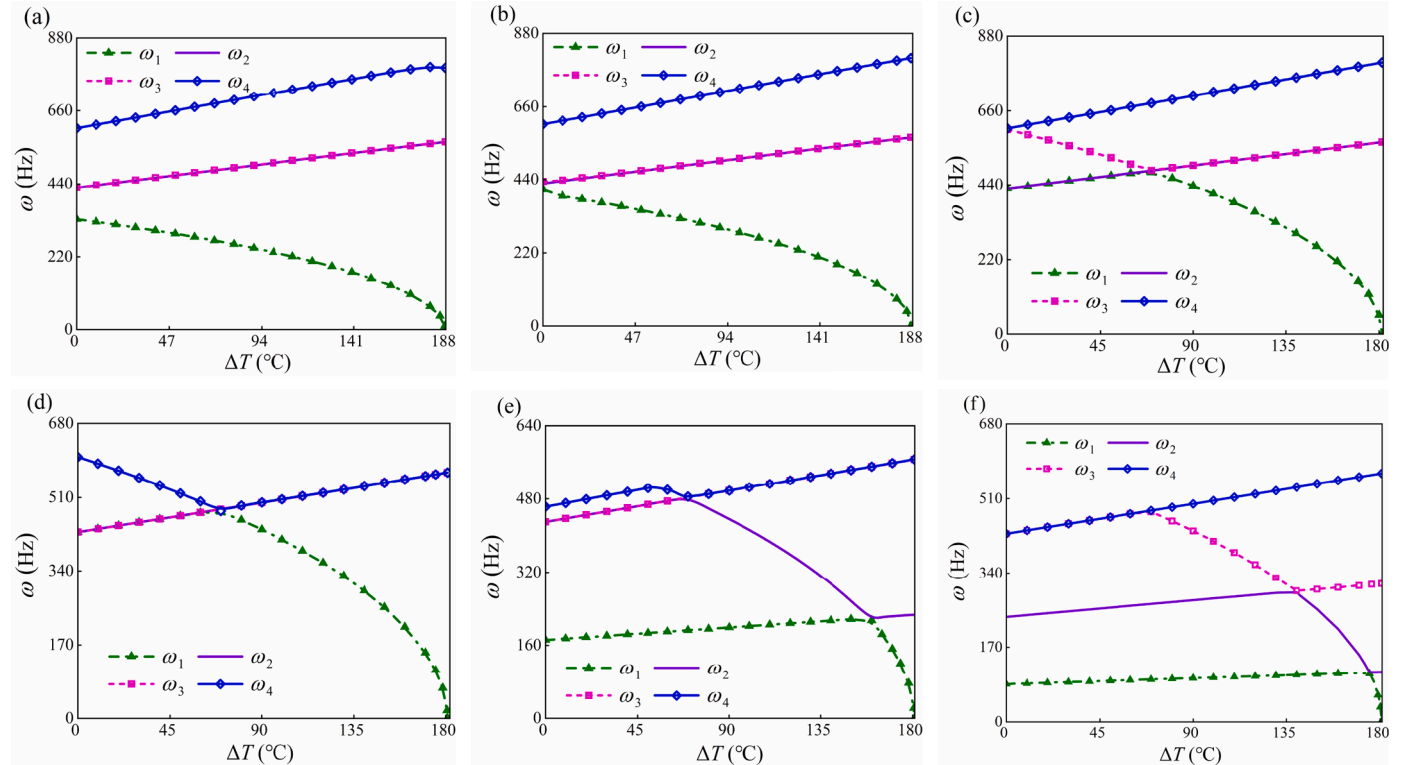


Fig. 5. Effect of temperature rise change both in structure and cavity on the first four orders  $\omega$  of the coupled system for  $a/h_p = 20$  under the different cavity depths: (a)  $h_c = 0.001$  m; (b)  $h_c = 0.0011$  m; (c)  $h_c = 0.01$  m; (d)  $h_c = 0.4$  m; (e)  $h_c = 1.0$  m; (f)  $h_c = 2.0$  m.

formula (15), compared to the non-enclosed case, the plate-controlled  $\omega$  is higher for the case of an enclosed cavity due to the higher medium density. Therefore, the CTR is larger when the plate-controlled  $\omega$  becomes zero. In other words, at the strong coupling stage, the increased medium density of the air-proofed cavity increases leads to an even larger CTR.

Similar calculations to Fig. 5 are carried out in Figs. 7 and 8. For the plate-cavity system with  $a/h_p = 100$ , where Fig. 7(a)–(c) correspond to strong coupling and Fig. 8(a)–(d) weak coupling. For Fig. 7(a)–(c), all first four  $\omega$  are plate-controlled and keep decreasing as  $\Delta T$  grows, with the two modes being identical in  $\omega$  since  $P(1,2) = P(2,1)$ . It is noted that the decreasing speed and the value of  $\omega$  are different, thus the mode shift phenomenon happens for different orders  $\omega$ . In Fig. 7(b), the mode shift phenomenon between the second and third modes is observed, and the first and second orders  $\omega$  become zero at  $\Delta T = 20.1^\circ\text{C}$ , which is very close to the second-order CTR of the rectangular plate ( $T_{cr}^2$ ), i.e., the CTR related to  $P(1,2)$  or  $P(2,1)$ . For Fig. 8(a), the first three  $\omega$  of the system are plate-controlled, while the fourth one is cavity-controlled, for  $\Delta T = 0$ . However, the first order  $\omega$  corresponds to  $P(1,1)$ , which becomes zero at  $\Delta T = 12.21^\circ\text{C}$ , which is larger than  $T_{cr}^1$  ( $\Delta T = 8.08^\circ\text{C}$ ) but smaller than  $T_{cr}^2$  ( $\Delta T = 20.1^\circ\text{C}$ ). For Fig. 8(b), (c), when the corresponding cavity depth is deep, more cavity-controlled  $\omega$  appears and remains nearly constant since  $\Delta T$  is not large, while the plate-controlled  $\omega$  decreases quickly with  $\Delta T$ . Calculation shows that the CTR is very close to  $T_{cr}^1$ .

Fig. 9 gives the CTR and the buckling mode shapes of the coupled system with respect to  $h_c$ . For shallow and strongly coupled plate-cavity systems, the CTR of the system is close to  $T_{cr}^2$ , with the buckling mode shape being anti-symmetric. For a deep plate-cavity system, the CTR is close to  $T_{cr}^1$ , with a symmetric buckling mode shape. For the depth that is in between, the CTR varies between  $T_{cr}^1$  and  $T_{cr}^2$ , and the buckling mode shape is largely symmetric. There is a critical case for  $h_c = 0.0033\text{ m}$ , the CTR of the symmetric buckling mode is the same as that of the anti-symmetric one. For this case, the symmetric  $\omega$  and the anti-symmetric  $\omega$  are not the same for  $\Delta T = 0$ , but decreases to zero at the same  $\Delta T$  due to their having different decreasing rate. Also, it is noted that  $T_{cr}^2$  is more than two times larger than that of  $T_{cr}^1$ , indicating that the CTR of the coupled system can be greatly increased due to the strong coupling effect, hence preventing the occurrence of buckling. Compared to Fig. 6, Fig. 9 plots a system with a thinner plate, whose enhancement in CTR is less obvious in magnitude. This difference is mainly because the CTR in the thin plate case varies in a much smaller range, hence the difference in terms of the CTR between the enclosed and non-enclosed cavity cases is not large.

#### 4. Concluding remarks

This work studies the modeling, thermal buckling, and vibro-acoustics of a plate-cavity system with general impedance boundaries exposed to a changing thermal environment, focusing on both weak and strong coupling cases and the way in which the plate-cavity coupling strengthens the thermal vibro-acoustics and buckling. Generally, the coupling is affected by structural geometry and the thermal effect. Strong coupling often happens for systems with thinner plates or shallow acoustic cavities, in which the coupled modes drastically differ from the uncoupled substructure or cavity. For example, for a shallow plate-cavity system that is strongly coupled, as the cavity becomes deeper, the coupled frequency that is related to the first/second order frequency of the uncoupled sub-plate, does not vary monotonically, but first increases quickly and then gradually decreases to the first/second order frequency of the uncoupled sub-plate. As the structure temperature increases, the equivalent structure is regarded to be even thinner, thus the system is more likely to be strongly coupled. For a plate with a higher temperature, the peak value of the coupled frequency is relatively smaller.

An interesting thermal buckling phenomenon in both weakly and strongly coupled plate-cavity systems is observed as the system temperature increases. For a sufficiently shallow cavity, the buckling mode of the coupled system actually corresponds to the second-order buckling mode of the uncoupled sub-plate. As the cavity gets deeper, the system gradually becomes weakly coupled, while the buckling mode of the coupled system gradually decreases to the first-order one of the uncoupled sub-plate. As a result, coupling the plate with a shallow cavity, can generally increase the critical buckling temperature rise, thus strengthening the system safety. This effect is even stronger if the cavity is air-proofed in which case the buckling temperature is high. Also, if the coupled cavity is shallow enough, the critical buckling temperature rise can even be times higher than that of the uncoupled sub-plate, due to the strong coupling effect, and the buckling mode shape can become anti-symmetric other than symmetric.

In practical applications, more complex structures and scenarios are involved. For example, various thermal factors such as thermal radiation, convective heat transfer, and heat conduction may affect the structural-cavity system, and complex non-uniform geometries are often encountered as well. Different heat transfer processes may cause complex heat distribution, either transient or steady-state, resulting in intricate thermal stresses and thermal works that are coupled to the system's vibration. It is worth investigating the vibro-acoustic and buckling mechanism of these transient or stable thermal scenarios, towards a better understanding and effective design of such systems. To achieve this, the existing methods may be extended whilst other methods such as finite element methods might need to be considered, especially for real-world applications.

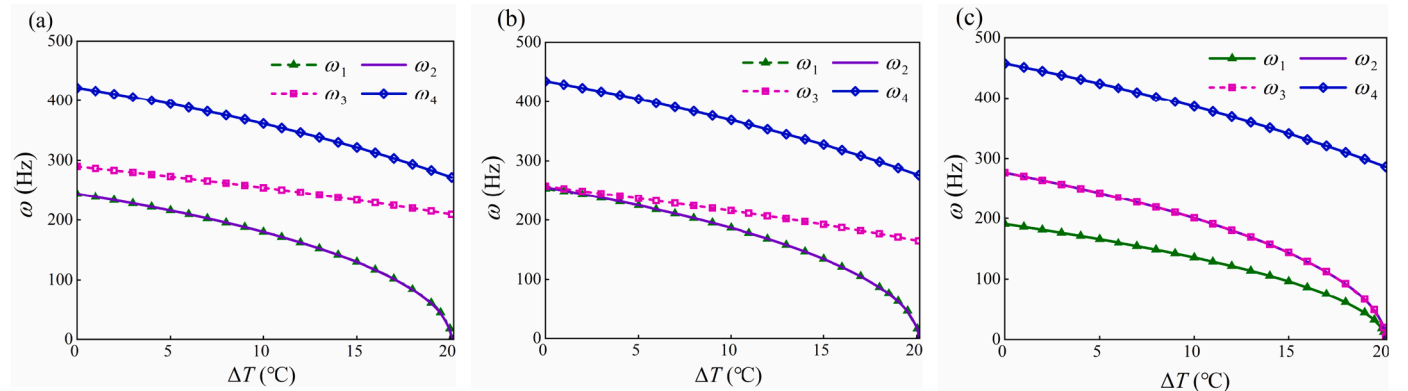
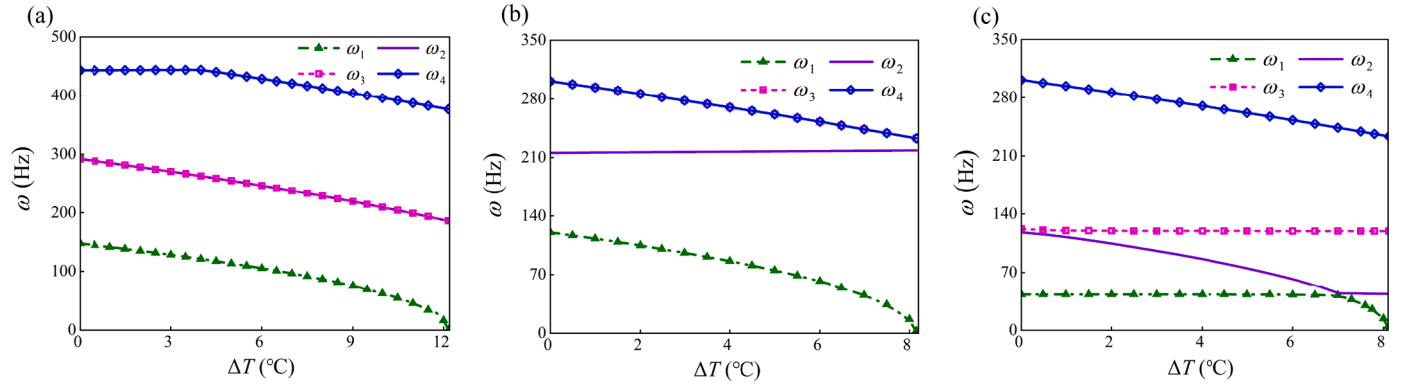
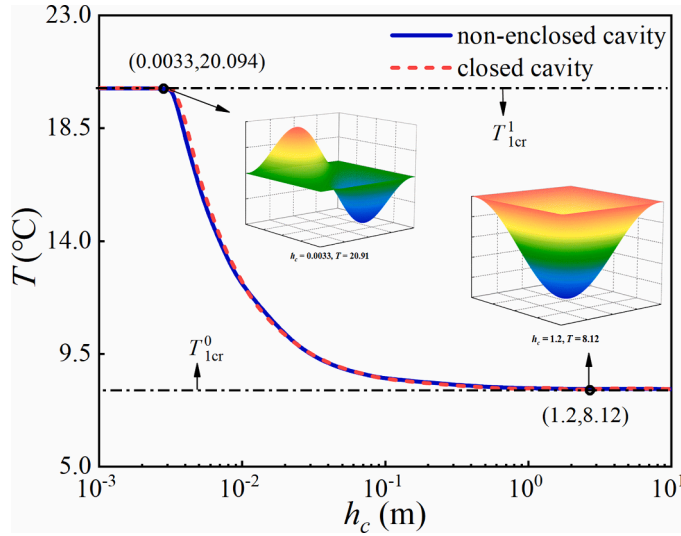


Fig. 7. Effect of temperature rise changes both in structure and cavity on the first four order  $\omega$  of the coupled system under strong coupling effect for  $a/h_p = 100$  under the different cavity depths: (a)  $h_c = 0.001\text{ m}$ ; (b)  $h_c = 0.0014\text{ m}$ ; (c)  $h_c = 0.0033\text{ m}$ .



**Fig. 8.** Effect of temperature rise changes both in structure and cavity on the first four order  $\omega$  of the coupled system under weak coupling effect for  $a/h_p = 100$  under the different cavity depths: (a)  $h_c = 0.01$  m; (b)  $h_c = 0.8$  m; (c)  $h_c = 4$  m.



**Fig. 9.** Effect of the cavity depth  $h_c$  on the critical buckling temperature rise of the coupled system with  $a/h_p = 100$ , for both enclosed and non-enclosed cases. The black dash line indicates the critical buckling temperature rise of the subsystem plate.

**CRediT authorship contribution statement**

**Qing Luo:** Conceptualization, Methodology, Software, Validation,

Investigation, Data curation, Writing – original draft, Formal analysis. **Yanfeng Wang:** Writing – review & editing, Investigation, Data curation, Formal analysis. **Yukang Yang:** Writing – review & editing, Investigation, Data curation. **Qi Xu:** Methodology, Writing – review & editing, Investigation, Data curation, Supervision, Funding acquisition. **Yinghui Li:** Methodology, Writing – review & editing, Supervision, Project administration, Funding acquisition. **Li Cheng:** Methodology, Writing – review & editing, Project administration, Funding acquisition.

**Declaration of Competing Interest**

The authors declare that they have no known competing financial interests or personal relationships that could have appeared to influence the work reported in this paper.

**Data availability**

Data will be made available on request.

**Acknowledgments**

This work is partially supported by the Research Grant Council of the Hong Kong SAR (PolyU 152036/18E), National Natural Science Foundation of China (Grant nos. 12272323, 12072292, 11702227), Natural Science Foundation of Sichuan Province (Grant no. 2022NSFSC0275).

**Appendix A. The energy function of the coupled system**

The potential energy  $U_p$  and the kinetic energy  $T_p$  of the plate takes the form of [76]

$$U_p = \frac{1}{2} \int_0^a \int_0^b \int_{-h_p/2}^{h_p/2} (\sigma_{xx}^0 \epsilon_{xx}^0 + \sigma_{yy}^0 \epsilon_{yy}^0 + \sigma_{xy}^0 \gamma_{xy}^0) dx dy dz,$$

$$T_p = \frac{\rho h \omega^2}{2} \int_0^a \int_0^b [U^2 + V^2 + W^2] dx dy$$

$$= \frac{\rho h \omega^2}{2} \int_0^a \int_0^b [u_0^2 + v_0^2 + w_0^2] dx dy + \frac{\rho \omega^2 h^3}{24} \int_0^a \int_0^b \left[ \left( \frac{\partial w_0}{\partial x} \right)^2 + \left( \frac{\partial w_0}{\partial y} \right)^2 \right] dx dy.$$

The energy terms of the acoustic cavity can be further expressed as

$$U_c = \frac{1}{2 \rho_c c_0^2} \int_0^a \int_0^b \int_0^{h_c} p^2 dx dy dz,$$

$$T_C = \frac{1}{2\rho_c\omega^2} \int_0^a \int_0^b \int_0^{h_c} \left[ \left( \frac{\partial p}{\partial x} \right)^2 + \left( \frac{\partial p}{\partial y} \right)^2 + \left( \frac{\partial p}{\partial z} \right)^2 \right] dx dy dz,$$

$$W_{P-C} = W_{C-P} = \int_s \left[ u_0 + v_0 + w_0 - z_e \left( \frac{\partial w_0}{\partial x} + \frac{\partial w_0}{\partial y} \right) \right] p \, ds,$$

$$W_{wall} = -\frac{1}{2} \int_{s_i} \sum_{i=1}^5 \frac{p^2}{j\omega Z_i} ds_i,$$

where  $s_i$  ( $i = 1, \dots, 5$ ) is the 5 walls of the cavity except the plate surface, and  $Z_i$  ( $i = 1, \dots, 5$ ) is the corresponding complex surface impedance.

**Appendix B. Matrices of governing equations**

To make the expressions easy and clear, some indexes are pre-defined:

$$\begin{aligned} s &= m(Np + 1) + n + 1, t = m'(Np + 1) + n' + 1, \\ S_1 &= m_1(Nc + 1)(Lc + 1) + n_1(Lc + 1) + l_1 + 1, T_1 = m'_1(Nc + 1)(Lc + 1) + n'_1(Lc + 1) + l'_1 + 1, \\ S_2 &= m_1(Nc + 1) + n_1 + 1, T_2 = m'_1(Nc + 1) + n'_1 + 1, \\ S_3 &= m_1(Lc + 1) + l_1 + 1, T_3 = m'_1(Lc + 1) + l'_1 + 1, \\ S_4 &= n_1(Lc + 1) + l_1 + 1, T_4 = n'_1(Lc + 1) + l'_1 + 1. \end{aligned}$$

Thus, the represented matrix  $K_P$  and  $C_{C-P}$  of the plate and their representative part are given as

$$K_P = \begin{bmatrix} K_{1-1} & K_{1-2} & K_{1-3} \\ K_{2-1} & K_{2-2} & K_{2-3} \\ K_{3-1} & K_{3-2} & K_{3-3} \end{bmatrix},$$

$$\begin{aligned} \{K_{1-1}\}_{s,t} &= \frac{1}{2} \int_0^a \int_0^b h_p \left[ \begin{aligned} &2Q_{11}\lambda_{am_i} \cos(\lambda_{am_i}x) \cos(\lambda_{bn_i}y) \lambda_{am} \cos(\lambda_{am}x) \cos(\lambda_{bn}y) \\ &+(Q_{11} - Q_{12})\lambda_{bn_i} \sin(\lambda_{am_i}x) \sin(\lambda_{bn_i}y) \lambda_{bn} \sin(\lambda_{am}x) \sin(\lambda_{bn}y) \end{aligned} \right] dx dy \\ &- 2 \int_0^a \int_0^b \Delta T a h_p \left[ \begin{aligned} &(Q_{12} + Q_{22})\lambda_{bn_i} \sin(\lambda_{am_i}x) \sin(\lambda_{bn_i}y) \lambda_{bn} \sin(\lambda_{am}x) \sin(\lambda_{bn}y) \\ &+(Q_{11} + Q_{12})\lambda_{am_i} \cos(\lambda_{am_i}x) \cos(\lambda_{bn_i}y) \lambda_{am} \cos(\lambda_{am}x) \cos(\lambda_{bn}y) \end{aligned} \right] dx dy, \end{aligned}$$

$$C_{C-P} = \begin{bmatrix} C_{1-1} & C_{1-2} & C_{1-3} & C_{1-4} & C_{1-5} & C_{1-6} & C_{1-7} \\ C_{2-1} & C_{2-2} & C_{2-3} & C_{2-4} & C_{2-5} & C_{2-6} & C_{2-7} \\ C_{3-1} & C_{3-2} & C_{3-3} & C_{3-4} & C_{3-5} & C_{3-6} & C_{3-7} \end{bmatrix},$$

$$\{C_{1-1}\}_{s,T_1} = \int_0^a \int_0^b \cos(\lambda_{am_i}x) \cos(\lambda_{bn_i}y) \cos(\lambda_{h_c l_1} z_e) \sin(\lambda_{am}x) \cos(\lambda_{bn}y) dx dy,$$

the material stiffness coefficients of the plate are given as

$$Q_{11} = Q_{22} = \frac{E}{(1 - \nu^2)}, Q_{12} = Q_{21} = \nu \frac{E}{(1 - \nu^2)}, Q_{66} = \frac{E}{2(1 + \nu)}.$$

Similarly, as to the acoustic cavity, the representative matrix  $Z_C$  and its part are given as follows

$$Z_C = \begin{bmatrix} Z_{1-1}^c & Z_{1-2}^c & Z_{1-3}^c & Z_{1-4}^c & Z_{1-5}^c & Z_{1-6}^c & Z_{1-7}^c \\ Z_{2-1}^c & Z_{2-2}^c & Z_{2-3}^c & Z_{2-4}^c & Z_{2-5}^c & Z_{2-6}^c & Z_{2-7}^c \\ Z_{3-1}^c & Z_{3-2}^c & Z_{3-3}^c & Z_{3-4}^c & Z_{3-5}^c & Z_{3-6}^c & Z_{3-7}^c \\ Z_{4-1}^c & Z_{4-2}^c & Z_{4-3}^c & Z_{4-4}^c & Z_{4-5}^c & Z_{4-6}^c & Z_{4-7}^c \\ Z_{5-1}^c & Z_{5-2}^c & Z_{5-3}^c & Z_{5-4}^c & Z_{5-5}^c & Z_{5-6}^c & Z_{5-7}^c \\ Z_{6-1}^c & Z_{6-2}^c & Z_{6-3}^c & Z_{6-4}^c & Z_{6-5}^c & Z_{6-6}^c & Z_{6-7}^c \\ Z_{7-1}^c & Z_{7-2}^c & Z_{7-3}^c & Z_{7-4}^c & Z_{7-5}^c & Z_{7-6}^c & Z_{7-7}^c \end{bmatrix},$$

$$\begin{aligned} \{Z_{-1}^c\}_{S_1, T_1} &= \frac{j}{Z_{z=h_c}} (-1)^{i_1+i_2} \int_0^a \int_0^b \cos(\lambda_{am_1} x) \cos(\lambda_{bn_1} y) \cos(\lambda_{am_1} x) \cos(\lambda_{bn_1} y) dx dy \\ &+ \frac{j}{Z_{x=0}} \int_0^b \int_0^{h_c} \cos(\lambda_{bn_1} y) \cos(\lambda_{hc, l_1} z) \cos(\lambda_{bn_1} y) \cos(\lambda_{hc, l_1} z) dy dz \\ &+ \frac{j}{Z_{x=a}} (-1)^{m_1+m_2} \int_0^b \int_0^{h_c} \cos(\lambda_{bn_1} y) \cos(\lambda_{bn_1} y) \cos(\lambda_{hc, l_1} z) \cos(\lambda_{hc, l_1} z) dy dz \\ &+ \frac{j}{Z_{y=0}} \int_0^a \int_0^{h_c} \cos(\lambda_{am_1} x) \cos(\lambda_{hc, l_1} z) \cos(\lambda_{am_1} x) \cos(\lambda_{hc, l_1} z) dx dz \\ &+ \frac{j}{Z_{y=b}} (-1)^{n_1+n_2} \int_0^a \int_0^{h_c} \cos(\lambda_{am_1} x) \cos(\lambda_{hc, l_1} z) \cos(\lambda_{am_1} x) \cos(\lambda_{hc, l_1} z) dx dz. \end{aligned}$$

Besides, the collection of unknown Fourier series coefficients  $\Theta$  and  $\Phi$  take the form of

$$\Theta = [A_{00}, \dots, A_{0n}, \dots, A_{mn}, \dots, A_{MN}, B_{00}, \dots, B_{0n}, \dots, B_{mn}, \dots, B_{MN}, C_{00}, \dots, C_{0n}, \dots, C_{mn}, \dots, C_{MN}]^T,$$

$$\Phi = \begin{bmatrix} D_{0,0,0}, \dots, D_{0,0,l_1}, \dots, D_{0,0,L_1}, \dots, D_{0,N_1,L_1}, \dots, D_{m_1,n_1,l_1}, \dots, D_{M_1N_1,L_1}, \\ D_{0,0}^1, \dots, D_{0,n_1}^1, \dots, D_{m_1,n_1}^1, \dots, D_{M_1,N_1}^1, D_{0,0}^2, \dots, D_{0,n_1}^2, \dots, D_{m_1,n_1}^2, \dots, D_{M_1,N_1}^2, \\ D_{0,0}^3, \dots, D_{0,l_1}^3, \dots, D_{m_1,l_1}^3, \dots, D_{M_1,L_1}^3, D_{0,0}^4, \dots, D_{0,l_1}^4, \dots, D_{m_1,l_1}^4, \dots, D_{M_1,L_1}^4, \\ D_{0,0}^5, \dots, D_{0,l_1}^5, \dots, D_{n_1,l_1}^5, \dots, D_{N_1,L_1}^5, D_{0,0}^6, \dots, D_{0,l_1}^6, \dots, D_{n_1,l_1}^6, \dots, D_{N_1,L_1}^6 \end{bmatrix}^T.$$

**Appendix C. Validation analysis**

The convergence and correctness of the modified Fourier series method are presented, by respectively calculating the natural frequencies of the subsystems, that is, a rectangular plate, a primary cavity, and a plate-cavity coupled system at room temperature.

**Table 1**

The convergence and accuracy of the first eight non-dimensional natural frequencies  $\Omega = \omega_p a^2 \sqrt{\rho_p/E_1 h_p^2}$  for the SUS304 plate at room temperature with its thickness is 0.005 m.

Mp × Np	mode number							
	1, P(1,1)	2, P(1,2)	3, P(2,1)	4, P(2,2)	5, P(1,3)	6, P(3,1)	7, P(2,3)	8, P(3,2)
2	19.739	49.348	49.348	78.957	–	–	–	–
3	19.739	49.348	49.348	78.957	98.696	98.696	128.305	128.305
4	19.739	49.348	49.348	78.957	98.696	98.696	128.305	128.305
5	19.739	49.348	49.348	78.957	98.696	98.696	128.305	128.305
6	19.739	49.348	49.348	78.957	98.696	98.696	128.305	128.305
7	19.739	49.348	49.348	78.957	98.696	98.696	128.305	128.305
8	19.739	49.348	49.348	78.957	98.696	98.696	128.305	128.305
9	19.739	49.348	49.348	78.957	98.696	98.696	128.305	128.305
Ref.[84]	19.739	49.349	49.349	79.401	100.173	100.186	130.389	–
Ref.[88]	19.74	49.35	49.35	78.96	98.70	98.70	–	–

**Table 2**

Convergence and accuracy of the first eight natural frequencies for the basic acoustic cavity with  $a/b = 1$ ,  $a = 0.4$  m,  $h_c = 0.25$  m under rigid walls.

Mc × Nc × Lc	mode number							
	1, S(0,1,0)	2, S(1,0,0)	3, S(1,1,0)	4, S(0,0,1)	5, S(0,1,1)	6, S(1,0,1)	7, S(0,2,0)	8, S(2,0,0)
3	430.002	430.002	608.115	688.002	811.325	811.325	860.002	860.002
4	430.003	430.003	608.115	688.003	811.325	811.325	860.003	860.003
5	430.003	430.003	608.115	688.002	811.325	811.325	860.003	860.003
6	430.003	430.003	608.115	688.002	811.325	811.325	860.003	860.003
7	430.003	430.003	608.115	688.002	811.325	811.325	860.003	860.003
8	430.003	430.003	608.115	688.002	811.325	811.325	860.003	860.003
Analytical [55]	430.000	430.000	608.112	688.000	811.322	811.322	860.000	860.000
FEM	430.000	430.000	608.120	688.011	811.342	811.342	860.020	860.020

Usually, the chosen truncation orders of the plate part are larger than those of the cavity part. In the following study, considering both the calculation precision and efficiency, truncation numbers  $M_p = N_p = 16$  and  $M_c = N_c = L_c = 6$  are adopted.

Table 3

Accuracy and validation comparison study of the first six natural frequencies for the brass plate coupled system with  $a/b = 1$ ,  $a = 0.2$  m,  $h_p = 0.9144$  mm.

Cavity depth	Methods	Model number					
		1	2	3	4	5	6
$hc = 0.02$	Present	145.02	193.04	193.04	310.55	389.12	394.43
	Ref. [78]	145.00	193.01	193.01	310.51	389.06	394.35
	Ref. [14]	143.85	193.00	193.00	310.47	388.90	394.08
	Ref. [89]	143.89	–	–	–	389.59	394.75
	Present	87.07	194.59	194.59	311.68	389.85	390.15
$hc = 0.2$	Ref. [78]	86.99	194.43	194.43	311.43	389.64	389.93
	Ref. [14]	86.78	194.44	194.44	311.40	389.47	389.74
	Ref. [89]	86.82	194.55	194.55	311.66	390.11	390.46
	Present	79.47	194.85	194.85	316.86	311.99	389.49
	Ref. [78]	79.42	194.45	194.45	216.84	311.48	389.02
$hc = 0.8$	Present	73.11	92.09	173.08	195.01	195.01	258.56
	Ref. [78]	72.81	91.89	173.09	194.54	194.54	258.56
	Ref. [14]	72.56	91.07	171.06	194.42	194.42	255.54
	Ref. [89]	72.58	91.08	171.05	–	–	255.54
	Present	78.08	195.15	195.15	312.24	390.31	390.31
<i>In-vacuo</i>	Analytical	78.06	195.15	195.15	312.24	390.31	390.31

## References

- [1] Chen L, Lu C, Lian H, Liu Z, Zhao W, Li S, et al. Acoustic topology optimization of sound absorbing materials directly from subdivision surfaces with isogeometric boundary element methods. *Comput Methods Appl Mech Eng* 2020;362:112806. <https://doi.org/10.1016/j.cma.2019.112806>.
- [2] Pirk R, d'Andrade C, Paulinelli G, Sandoval Ges LC. Acoustics and vibro-acoustics applied in space industry. *Model Meas Methods Acoust Waves Acoust Microdevices* 2013. <https://doi.org/10.5772/49966>.
- [3] Dobrzynski W. Almost 40 years of airframe noise research: what did we achieve? *J Aircr* 2010;47:353–67. <https://doi.org/10.2514/1.44457>.
- [4] Ansari R, Torabi J, Hassani R. Thermal buckling analysis of temperature-dependent FG-CNTRC quadrilateral plates. *Comput Math Appl* 2019;77:1294–311. <https://doi.org/10.1016/j.camwa.2018.11.009>.
- [5] Yang Y, Luo Q, an Li J, Dong Y, Chen B, Li Y. Symmetric and asymmetric thermo-induced buckling and postbuckling of rotating GPLRC annular plates rested on elastic foundation. *Eng Struct* 2022;259. <https://doi.org/10.1016/j.engstruct.2022.114110>.
- [6] Chen B, Xu Q, Zhu B, Yang Y, Li Y. Buckling and postbuckling behaviors of symmetric/asymmetric double-beam systems. *Int J Mech Sci* 2022;235. <https://doi.org/10.1016/j.ijmecsci.2022.107712>.
- [7] Fahy FJ. Vibration of containing structures by sound in the contained fluid. *J Sound Vib* 1969;10:490–512. [https://doi.org/10.1016/0022-460X\(69\)90228-4](https://doi.org/10.1016/0022-460X(69)90228-4).
- [8] Pan J, Bies DA. The effect of fluid-structural coupling on sound waves in an enclosure—Theoretical part. *J Acoust Soc Am* 1990;87:691–707. <https://doi.org/10.1121/1.398939>.
- [9] Park SY, Kim SH, Kang YJ. The effect of a local stiffener in the structural-acoustic coupled system. *Proc Inst Mech Eng Part C* 2010;224:1915–31. <https://doi.org/10.1243/09544062JMES1744>.
- [10] Maxit L. Analysis of the modal energy distribution of an excited vibrating panel coupled with a heavy fluid cavity by a dual modal formulation. *J Sound Vib* 2013;332:6703–24. <https://doi.org/10.1016/j.jsv.2013.07.020>.
- [11] Maxit L, Guyader JL. Estimation of SEA coupling loss factors using a dual formulation and FEM modal information, Part I: theory. *J Sound Vib* 2001;239:907–30. <https://doi.org/10.1006/jsvi.2000.3192>.
- [12] Srinivasan Puri R, Morrey D, Bell AJ, Durodola JF, Rudnyi EB, Korvink JG. Reduced order fully coupled structural-acoustic analysis via implicit moment matching. *Appl Math Model* 2009;33:4097–119. <https://doi.org/10.1016/j.apm.2009.02.016>.
- [13] Bai Z. Krylov subspace techniques for reduced-order modeling of large-scale dynamical systems. *Appl Numer Math* 2002;43:9–44. [https://doi.org/10.1016/S0168-9274\(02\)00116-2](https://doi.org/10.1016/S0168-9274(02)00116-2).
- [14] Xie X, Zheng H, Qu Y. A variational formulation for vibro-acoustic analysis of a panel backed by an irregularly-bounded cavity. *J Sound Vib* 2016;373:147–63. <https://doi.org/10.1016/j.jsv.2016.03.003>.
- [15] Cessenat O, Després B. Using plane waves as base functions for solving time harmonic equations with the ultra weak variational formulation. *J Comput Acoust* 2003;11:227–38. <https://doi.org/10.1142/S0218396X03001912>.
- [16] Lei Y, Pan J, Sheng MP. Investigation of structural response and noise reduction of an acoustical enclosure using SEA method. *Appl Acoust* 2012;73:348–55. <https://doi.org/10.1016/j.apacoust.2011.10.008>.
- [17] Maxit L, Guyader JL. Extension of SEA model to subsystems with non-uniform modal energy distribution. *J Sound Vib* 2003;265:337–58. [https://doi.org/10.1016/S0022-460X\(02\)01459-1](https://doi.org/10.1016/S0022-460X(02)01459-1).
- [18] Egab L, Wang X. On the analysis of coupling strength of a stiffened plate-cavity coupling system using a deterministic-statistical energy analysis method. *Mech Syst Signal Process* 2022;164:108234. <https://doi.org/10.1016/j.ymssp.2021.108234>.
- [19] Mohamed Z, Wang X. A deterministic and statistical energy analysis of tyre cavity resonance noise. *Mech Syst Signal Process* 2016;70–71:947–57. <https://doi.org/10.1016/j.ymssp.2015.09.012>.
- [20] Renji K, Nair PS, Narayanan S. Non-resonant response using statistical energy analysis. *J Sound Vib* 2001;241:253–70. <https://doi.org/10.1006/jsvi.2000.3270>.
- [21] Du JT, Li WL, Xu HA, Liu ZG. Vibro-acoustic analysis of a rectangular cavity bounded by a flexible panel with elastically restrained edges. *J Acoust Soc Am* 2012;131:2799–810. <https://doi.org/10.1121/1.3693652>.
- [22] Zhang X, Cheng L, Liu Y, Du J. Acoustic modelling and analyses of geometrically complex systems with Micro-perforated panels. *J Sound Vib* 2021;499. <https://doi.org/10.1016/j.jsv.2021.115995>.
- [23] Zhang H, Shi D, Wang Q, Zha S. Vibro-acoustic analysis of the annular segment flexible plate coupled with an impedance walled enclosure. *Thin-Walled Struct* 2018;131:205–22. <https://doi.org/10.1016/j.tws.2018.07.002>.
- [24] Shi SX, Jin GY, Liu ZG. Vibro-acoustic behaviors of an elastically restrained double-panel structure with an acoustic cavity of arbitrary boundary impedance. *Appl Acoust* 2014;76:431–44. <https://doi.org/10.1016/j.apacoust.2013.09.008>.
- [25] Kong D, Wang G. Analytical coupled vibro-acoustic modeling of tensioned membrane backed by the rectangular cavity. *Int J Mech Sci* 2022;227:107462. <https://doi.org/10.1016/j.ijmecsci.2022.107462>.
- [26] Chen Y, Jin G, Feng Z, Liu Z. Modeling and vibro-acoustic analysis of elastically restrained panel backed by irregular sound space. *J Sound Vib* 2017;409:201–16. <https://doi.org/10.1016/j.jsv.2017.07.053>.
- [27] Jin GY, Chen YH, Liu ZG. A Chebyshev-Lagrangian method for acoustic analysis of a rectangular cavity with arbitrary impedance walls. *Appl Acoust* 2014;78:33–42. <https://doi.org/10.1016/j.apacoust.2013.10.015>.
- [28] Chappell DJ, Giani S, Tanner G. Dynamical energy analysis for built-up acoustic systems at high frequencies. *J Acoust Soc Am* 2011;130:1420–9. <https://doi.org/10.1121/1.3621041>.
- [29] Van Genechten B, Vandepitte D, Desmet W. A direct hybrid finite element - wave based modelling technique for efficient coupled vibro-acoustic analysis. *Comput Methods Appl Mech Eng* 2011;200:742–64. <https://doi.org/10.1016/j.cma.2010.09.017>.
- [30] Harari I, Grosh K, Hughes TJR, Malhotra M, Pinsky PM, Stewart JR, et al. Recent developments in finite element methods for structural acoustics. *Arch Comput Methods Eng* 1996;3:131–309. <https://doi.org/10.1007/BF03041209>.
- [31] Chappell DJ, Tanner G, Giani S. Boundary element dynamical energy analysis: a versatile method for solving two or three dimensional wave problems in the high frequency limit. *J Comput Phys* 2012;231:6181–91. <https://doi.org/10.1016/j.jcp.2012.05.028>.
- [32] Djojodihardjo H. Vibro-acoustic analysis of the acoustic-structure interaction of flexible structure due to acoustic excitation. *Acta Astronaut* 2015;108:129–45. <https://doi.org/10.1016/j.actaastro.2014.11.026>.
- [33] Hell S, Becker W. Energy release rates at two perpendicularly meeting cracks by use of the scaled boundary finite element method. *Procedia Struct Integr* 2016;2:2471–8. <https://doi.org/10.1016/j.prostr.2016.06.309>.
- [34] Park J, Park I, Lee U. Transverse vibration and waves in a membrane: frequency domain spectral element modeling and analysis. *Math Probl Eng* 2014;2014. <https://doi.org/10.1155/2014/642782>.
- [35] Antonietti PF, Bonaldi F, Mazzieri I. Simulation of three-dimensional elastoacoustic wave propagation based on a discontinuous Galerkin spectral element method. *Int J Numer Methods Eng* 2020;121:2206–26. <https://doi.org/10.1002/nme.6305>.
- [36] Mencik JM. On the low- and mid-frequency forced response of elastic structures using wave finite elements with one-dimensional propagation. *Comput Struct* 2010;88:674–89. <https://doi.org/10.1016/j.compstruc.2010.02.006>.

- [37] van Genechten B, Plumers B, Vandepitte D, Desmet W. A hybrid wave based - modally reduced finite element method for the efficient analysis of low- and mid-frequency car cavity acoustics. *SAE Int J Passeng Cars - Mech Syst* 2009;2: 1494–504. <https://doi.org/10.4271/2009-01-2214>.
- [38] Atak O, Jonckheere S, Deckers E, Huybrechs D, Plumers B, Desmet W. A hybrid boundary element-wave based method for an efficient solution of bounded acoustic problems with inclusions. *Comput Methods Appl Mech Eng* 2015;283:1260–77. <https://doi.org/10.1016/j.cma.2014.08.019>.
- [39] Bouillard P, Ihlenburg F. Error estimation and adaptivity for the finite element method in acoustics: 2D and 3D applications. *Comput Methods Appl Mech Eng* 1999;176:147–63. [https://doi.org/10.1016/S0045-7825\(98\)00334-X](https://doi.org/10.1016/S0045-7825(98)00334-X).
- [40] Desmet W. A wave-based prediction technique for coupled vibro-acoustic analysis. *Katholieke Universiteit Leuven*; 1998.
- [41] Dhandole SD, Modak SV. A comparative study of methodologies for vibro-acoustic FE model updating of cavities using simulated data. *Int J Mech Mater Des* 2010;6: 27–43. <https://doi.org/10.1007/s10999-010-9116-4>.
- [42] Hu Z, Maxit L, Cheng L. Mid-to-high frequency piecewise modelling of an acoustic system with varying coupling strength. *Mech Syst Signal Process* 2019;134: 106312. <https://doi.org/10.1016/j.ymssp.2019.106312>.
- [43] Hu Z, Maxit L, Cheng L. Piecewise convergence behavior of the condensed transfer function approach for mid-to-high frequency modelling of a panel-cavity system. *J Sound Vib* 2018;435:119–34. <https://doi.org/10.1016/j.jsv.2018.08.010>.
- [44] Li YY, Cheng L. Modifications of acoustic modes and coupling due to a leaning wall in a rectangular cavity. *J Acoust Soc Am* 2004;116:3312–8. <https://doi.org/10.1121/1.1823331>.
- [45] Shen YX, Peng YG, Zhao DG, Chen XC, Zhu J, Zhu XF. One-way localized adiabatic passage in an acoustic system. *Phys Rev Lett* 2019;122:94501. <https://doi.org/10.1103/PhysRevLett.122.094501>.
- [46] Liao J, Zhu H, Hou J, Yuan S. Study on acoustic characteristics of a flexible plate strongly coupled with rectangular cavity. *Shock Vib* 2021;2021. <https://doi.org/10.1155/2021/5565136>.
- [47] Tournour M, Atalla N. Pseudostatic corrections for the forced vibroacoustic response of a structure-cavity system. *J Acoust Soc Am* 2000;107:2379–86. <https://doi.org/10.1121/1.428624>.
- [48] Aucejo M, Maxit L, Totaro N, Guyader JL. Convergence acceleration using the residual shape technique when solving structure-acoustic coupling with the patch transfer functions method. *Comput Struct* 2010;88:728–36. <https://doi.org/10.1016/j.compstruc.2010.02.010>.
- [49] David JM, Menelle M. Validation of a modal method by use of an appropriate static potential for a plate coupled to a water-filled cavity. *J Sound Vib* 2007;301: 739–59. <https://doi.org/10.1016/j.jsv.2006.10.033>.
- [50] Kim SM, Kim JG, Chae SW, Park KC. A strongly coupled model reduction of vibro-acoustic interaction. *Comput Methods Appl Mech Eng* 2019;347:495–516. <https://doi.org/10.1016/j.cma.2018.12.029>.
- [51] Griffin S, Lane SA, Hansen C, Cazzolato B. Active structural-acoustic control of a rocket fairing using proof-mass actuators. *J Spacecr Rockets* 2001;38:219–25. <https://doi.org/10.2514/2.3673>.
- [52] Eustice RM, Whitcomb LL, Singh H, Grund M. Experimental results in synchronous-clock one-way-travel-time acoustic navigation for autonomous underwater vehicles. *Proc - IEEE Int Conf Robot Autom* 2007;4257–64. <https://doi.org/10.1109/ROBOT.2007.364134>.
- [53] Fuchs M. Heat flux. *Methods of Soil Analysis. Part I. Physical and Mineralogical Methods*. Madison, Wisconsin, USA: American Society of Agronomy; 1986. p. 957–68. <https://doi.org/10.2136/sssabookser5.1.2ed.c40>.
- [54] Arai N, Matsunami A, Churchill SW. A review of measurements of heat flux density applicable to the field of combustion. *Exp Therm Fluid Sci* 1996;12:452–60. [https://doi.org/10.1016/0894-1777\(95\)00136-0](https://doi.org/10.1016/0894-1777(95)00136-0).
- [55] Boyer TH. Blackbody radiation in classical physics: a historical perspective. *Am J Phys* 2018;86:495–509. <https://doi.org/10.1119/1.5034785>.
- [56] Mondol A, Gupta R, Das S, Dutta T. An insight into Newton's cooling law using fractional calculus. *J Appl Phys* 2018;123. <https://doi.org/10.1063/1.4998236>.
- [57] Sazhin SS, Gol'dshteyn VA, Heikal MR. A transient formulation of Newton's cooling law for spherical bodies. *J Heat Transf* 2001;123:63–4. <https://doi.org/10.1115/1.1337650>.
- [58] Chandra A, Chhabra RP. Effect of Prandtl number on natural convection heat transfer from a heated semi-circular cylinder. *Int J Mech Mechatron Eng* 2012;6: 146–52.
- [59] Chen S, Wang J, Casati G, Benenti G. Nonintegrability and the Fourier heat conduction law. *Phys Rev E* 2014;90:1–5. <https://doi.org/10.1103/PhysRevE.90.032134>.
- [60] Nesarhosseini S, Ansari R, Faraji Oskouie M, Rouhi H. Thermally induced vibration analysis of Timoshenko beams based on the micropolar thermoelasticity. *Acta Mech* 2023;234:1957–71. <https://doi.org/10.1007/s00707-022-03455-5>.
- [61] Li J, Yan S. Thermally induced vibration of composite solar array with honeycomb panels in low earth orbit. *Appl Therm Eng* 2014;71:419–32. <https://doi.org/10.1016/j.applthermaleng.2014.07.015>.
- [62] Srikanth S, Sahay A, Pawar SA, Manoj K, Sujith RI. Self-coupling: an effective method to mitigate thermoacoustic instability. *Nonlinear Dyn* 2022;110:2247–61. <https://doi.org/10.1007/s11071-022-07750-7>.
- [63] Liu T, Li J, Zhu S, Yang L. Determination of the heat conduction transfer function within the thermoacoustic instability limit cycle in a Rijke tube. *Appl Therm Eng* 2022;206:118084. <https://doi.org/10.1016/j.applthermaleng.2022.118084>.
- [64] Chen Q, Fei Q, Devriendt H, Wu S, Plumers B, Desmet W. Investigation of thermal effects on the steady-state vibrations of a rectangular plate-cavity system subjected to harmonic loading and static temperature loads using a wave based method. *Wave Motion* 2021;104:102748. <https://doi.org/10.1016/j.wavemoti.2021.102748>.
- [65] Li X, Yu K. Vibration and acoustic responses of composite and sandwich panels under thermal environment. *Compos Struct* 2015;131:1040–9. <https://doi.org/10.1016/j.compstruct.2015.06.037>.
- [66] Li Z, Wang Q, Qin B, Zhong R, Yu H. Vibration and acoustic radiation of magneto-electro-thermo-elastic functionally graded porous plates in the multi-physics fields. *Int J Mech Sci* 2020;185. <https://doi.org/10.1016/j.ijmesci.2020.105850>.
- [67] Gunasekaran V, Pitchaimani J, Mailan Chinnapandi LB. Acoustic radiation and transmission loss of FG-graphene composite plate under nonuniform edge loading. *Eur J Mech A/Solids* 2021;88:104249. <https://doi.org/10.1016/j.euromechsol.2021.104249>.
- [68] Álvarez JG, Abramovich H, Bisagni C. Vibration-buckling tests on heated composite plates. *J Sound Vib* 2022;536. <https://doi.org/10.1016/j.jsv.2022.117145>.
- [69] Murphy KD, Ferreira D. Thermal buckling of rectangular plates. *Int J Solids Struct* 2001;38:3979–94. [https://doi.org/10.1016/S0020-7683\(00\)00240-7](https://doi.org/10.1016/S0020-7683(00)00240-7).
- [70] Sohn KJ, Kim JH. Nonlinear thermal flutter of functionally graded panels under a supersonic flow. *Compos Struct* 2009;88:380–7. <https://doi.org/10.1016/j.compstruct.2008.04.016>.
- [71] Song WS, Lee S, Shin DS, Na Y. Thermo-acoustic instability in the horizontal rijke tube. *J Mech Sci Technol* 2006;20:905–13. <https://doi.org/10.1007/BF02915953>.
- [72] Shimpi RP. Refined plate theory and its variants. *AIAA J* 2002;40:137–46. <https://doi.org/10.2514/2.1622>.
- [73] Latifi M, Farhatnia F, Kadkhodaei M. Buckling analysis of rectangular functionally graded plates under various edge conditions using Fourier series expansion. *Eur J Mech A/Solids* 2013;41:16–27. <https://doi.org/10.1016/j.euromechsol.2013.01.008>.
- [74] Zhang H, Zhu R, Shi D, Wang Q, Yu H. Study on vibro-acoustic property of composite laminated rotary plate-cavity system based on a simplified plate theory and experimental method. *Int J Mech Sci* 2020;167. <https://doi.org/10.1016/j.ijmesci.2019.105264>.
- [75] Reddy JN. *Theory and analysis of elastic plates and shells*. CRC Press; 2006. <https://doi.org/10.1201/9780849384165>.
- [76] Xing YF, Wang ZK, Xu TF. Closed-form analytical solutions for free vibration of rectangular functionally graded thin plates in thermal environment. *Int J Appl Mech* 2018;10. <https://doi.org/10.1142/S1758825118500254>.
- [77] Alijani F, Bakhtiari-Nejad F, Amabili M. Nonlinear vibrations of FGM rectangular plates in thermal environments. *Nonlinear Dyn* 2011;66:251–70. <https://doi.org/10.1007/s11071-011-0049-8>.
- [78] Zhang H, Shi D, Zha S, Wang Q. Vibro-acoustic analysis of the thin laminated rectangular plate-cavity coupling system. *Compos Struct* 2018;189:570–85. <https://doi.org/10.1016/j.compstruct.2018.01.099>.
- [79] Li F, Chen Y, Lv M. Vibro-acoustic characteristics of sigmoid functionally graded sandwich plates with temperature-dependent materials. *Thin-Walled Struct* 2021; 159:107310. <https://doi.org/10.1016/j.tws.2020.107310>.
- [80] Li FL, Yuan W, Lv M. Buckling and vibro-acoustic characteristics of the trapezoidal corrugated sandwich plate in thermal environment. *J Therm Stress* 2021;44: 807–28. <https://doi.org/10.1080/01495739.2021.1919584>.
- [81] Zhang H, Shi D, Zha S, Wang Q. Results in Physics Sound-vibration behaviors of the thin orthotropic rectangular fluid - structure coupled system resting on varying elastic Winkler and Pasternak foundations. *Results Phys* 2018;11:188–200. <https://doi.org/10.1016/j.rinp.2018.09.002>.
- [82] Lei Z, Su Q, Zeng H, Zhang Y, Yu C. Parametric studies on buckling behavior of functionally graded graphene-reinforced composites laminated plates in thermal environment. *Compos Struct* 2018;202:695–709. <https://doi.org/10.1016/j.compstruct.2018.03.079>.
- [83] Du JT, Li WL, Liu ZG, Xu HA, Ji ZL. Acoustic analysis of a rectangular cavity with general impedance boundary conditions. *J Acoust Soc Am* 2011;130:807–17. <https://doi.org/10.1121/1.3605534>.
- [84] Chakraverty S, Pradhan KK. Free vibration of exponential functionally graded rectangular plates in thermal environment with general boundary conditions. *Aerosp Sci Technol* 2014;36:132–56. <https://doi.org/10.1016/j.ast.2014.04.005>.
- [85] Li MM, Song FZ, Ding CG. The frequency veering phenomena of the beams of cantilever screen. *Appl Mech Mater* 2012;226–228:580–3. <https://doi.org/10.4028/www.scientific.net/AMM.226-228.580>.
- [86] Fang J, Yin B, Zhang X. Size-dependent vibrations of porous functionally graded rotating microplates under thermal environment. *Eur J Mech A/Solids* 2022;95: 104645. <https://doi.org/10.1016/j.euromechsol.2022.104645>.
- [87] Cheng L, Nicolas J. Radiation of sound into a cylindrical enclosure from a point-driven end plate with general boundary conditions. *J Acoust Soc Am* 1992;91: 1504–13. <https://doi.org/10.1121/1.402482>.
- [88] Li WL. Vibration analysis of rectangular plates with general elastic boundary supports. *J Sound Vib* 2004;273:619–35. [https://doi.org/10.1016/S0022-460X\(03\)00562-5](https://doi.org/10.1016/S0022-460X(03)00562-5).
- [89] Guy RW. Steady state transmission of sound at normal and oblique incidence through a thin panel backed by a rectangular room—A multi-modal analysis. *Acustica* 1979;43:295–304.